Case study of bilayered spin-$\frac{1}{2}$ square lattice compound $VO(HCOO)_2 \cdot (H_2O)$

S. Guchhait,[1] U. Arjun,[1] P. K. Anjana,[2] M. Sahoo,[3] A. Thirumurugan,[2] A. Medhi,[1] Y. Skourski,[4] B. Koo,[5] J. Sichelschmidt,[5]
B. Schmidt,[5] M. Baenitz,[5] and R. Nath[1,*]
[1]*School of Physics, Indian Institute of Science Education and Research Thiruvananthapuram-695551, India*
[2]*School of Chemistry, Indian Institute of Science Education and Research Thiruvananthapuram-695551, India*
[3]*Department of Physics, University of Kerala, Kariavattom, Thiruvananthapuram-695581, India*
[4]*Dresden High Magnetic Field Laboratory (HLD-EMFL), Helmholtz-Zentrum Dresden-Rossendorf, 01328 Dresden, Germany*
[5]*Max Planck Institute for Chemical Physics of Solids, Nthnitzer Str. 40, 01187 Dresden, Germany*

(Received 19 July 2019; published 14 October 2019)

We present the synthesis and a detailed investigation of structural and magnetic properties of polycrystalline $VO(HCOO)_2 \cdot (H_2O)$ by means of x-ray diffraction, magnetic susceptibility, high-field magnetization, heat capacity, and electron-spin-resonance measurements. The compound crystallizes in an orthorhombic structure with space group *Pcca*. The crystal lattice features distorted VO_6 octahedra connected via HCOO linkers (formate anions), forming a two-dimensional square lattice network with a bilayered structure. Analysis of magnetic susceptibility, high-field magnetization, and heat capacity data in terms of the frustrated square lattice model unambiguously establish the quasi-two-dimensional nature of the compound with nearest-neighbor interaction $J_1/k_B \simeq 11.7$ K and next-nearest-neighbor interaction $J_2/k_B \simeq 0.02$ K. A Néel antiferromagnetic ordering sets in at $T_N \simeq 1.1$ K. The ratio $\theta_{CW}/T_N \simeq 10.9$ reflects excellent two-dimensionality of the spin-lattice in the compound. A strong in-plane anisotropy is inferred from the linear increase of T_N with magnetic field, consistent with the structural data.

DOI: 10.1103/PhysRevMaterials.3.104409

I. INTRODUCTION

Over the past decades, two-dimensional (2D) antiferromagnetic (AFM) spin-1/2 systems have played an important role to understand the phase transitions and critical phenomena in magnetic materials [1]. The thermodynamic properties of such systems are nowadays well established by extensive numerical studies [2–4]. The ideal 2D Heisenberg antiferromagnets conventionally lack long-range order (LRO) down to zero temperature, following the Mermin-Wagner theorem [5]. But real materials inevitably possess a non-negligible interplane coupling that triggers the LRO at a finite temperature [6]. When the interplane couplings are frustrated and inactive, the LRO is driven by anisotropy terms in the spin Hamiltonian. In addition to the frustrated interplane couplings, competing interactions [e.g., nearest-neighbor interaction (J_1) along the edge with next-nearest-neighbor interaction (J_2) along the diagonal of the square] in spin-1/2 2D systems, known as the $J_1 - J_2$ model, often destabilize LRO, giving rise to various nonmagnetic ground states [7–11]. Even in high-T_c cuprates, the 2D AFM correlations are believed to be an essential ingredient for superconductivity [1,12]. Most interestingly, a recent report by Jain *et al.* [13] suggests that a condensed-matter analog for the physics of Higgs boson decay, which is very important in particle physics, can be provided by 2D AFM materials. It is anticipated that condensed matter realization of Higgs boson can provide insights regarding its behavior in different symmetries and dimensionalities [14].

Though there are numerous experimental studies on spin-1/2 square lattices, the majority of them are focused on purely inorganic systems and only few studies are reported on metal-organic based materials. The advantage of these metal-organic systems is that one can tune their physical properties simply by changing the organic ligands [15]. Second, metal-organic complexes have relatively weak exchange couplings compared to the inorganic compounds, which makes them promising candidates for high-field experiments, especially to explore the field-induced quantum phenomenon [11,16,17]. An interesting example of this category is $Cu(pz)_2(ClO_4)_2$, which has attracted a lot more attention experimentally as well as theoretically [11,18–20]. Layered metal-organic complexes also exhibit various peculiar electronic properties such as metal-insulator transition, Fermi liquid behavior, unconventional superconductivity, etc. [21–24]. Unlike inorganic compounds, the mechanism behind all these phenomenon in organic-based metal complexes is not yet understood. Therefore, recently, there is an enduring demand to synthesize metal-organic-based spin-1/2 2D model compounds and investigate the physical properties to elucidate their relevance in strongly correlated physics.

In this paper, we present the magnetic properties of a spin-1/2 quasi-2D AFM compound, $VO(HCOO)_2 \cdot (H_2O)$, investigated via magnetic susceptibility, high-field magnetization, heat capacity, and electron-spin-resonance (ESR) measurements. The vanadyl formate $VO(HCOO)_2 \cdot (H_2O)$ crystallizes in an orthorhombic structure with space group *Pcca* [25]. As

---

[*] rnath@iisertvm.ac.in

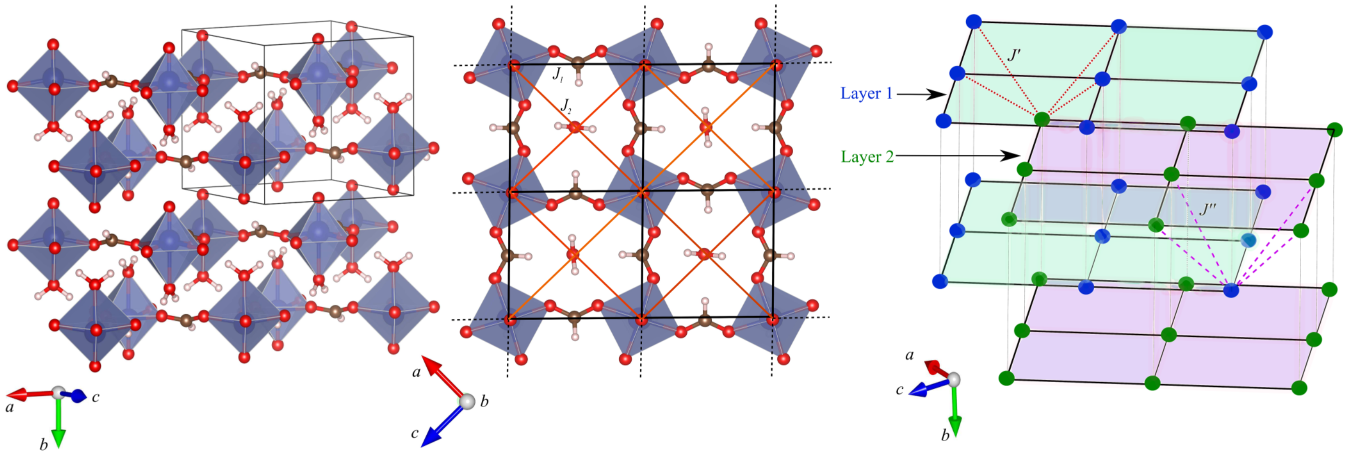

FIG. 1. Left panel: Three-dimensional view of the crystal structure showing VO$(HCOO)_2$ double layers lying perpendicular to the *b* axis. Middle panel: A section of one layer in the *ac* plane, showing a square lattice of VO_6 octahedra connected through HCOO bridges and the frustrated square lattice or the $J_1 - J_2$ model. Right panel: Spin lattice showing two layers and possible exchange couplings between the layers.

shown in the left panel of Fig. 1, the unit cell contains two VO$(HCOO)_2$ layers which are interdigitated by coordinated water molecules to form a bilayer system. The bilayers are repeated along the *b* direction to form a three-dimensional (3D) structure. In each VO$(HCOO)_2$ layer, a 2D square lattice network is formed by the distorted VO_6 octahedra linked via HCOO bridges. The distance between V^{4+} ions along the edges of the square is found to be ~5.977 Å and are coupled with an exchange coupling J_1, as shown in the middle panel of Fig. 1. There is no visible connecting path among the V^{4+} ions along the diagonals of the square. Therefore, the interaction along the diagonals (J_2) is expected to be very weak. It was further observed that the distance between the V^{4+} ions along the diagonals of the square are different, i.e., ~8.395 Å and ~8.51 Å. This inequality may produce a strong in-plane anisotropy in the compound. Similarly, there is no bonding between the interlayer vanadyl groups and hence, the interlayer interactions, if at all present, should be negligible compared to the intralayer interactions.

The right panel of Fig. 1 presents a schematic view of the spin lattice with a possible exchange network between the layers. One can see that vanadyl groups of layer 1 may interact with that of layer 2 (separated by a distance of ~5.41 Å) in a triangular fashion with exchange coupling J'. Similarly, vanadyl group of layer 2 may interact with that of the next layer 1 (separated by a distance of ~5.86 Å) in a triangular fashion with exchange coupling J''. The frustrated triangular network between the layers is expected to suppress the LRO to very low temperatures, retaining the two-dimensionality of the system over a large temperature range. Thus, the bilayered nature and the frustrated triangular interlayer interactions make VO$(HCOO)_2 \cdot (H_2O)$ an unusual candidate compared to other 2D compounds.

Our magnetic measurements reveal that VO$(HCOO)_2 \cdot (H_2O)$ is a spin-1/2 square-lattice compound with $J_1 \simeq 11.7$ K and $J_2 \simeq 0.02$ K. The onset of a Néel AFM ordering occurs at $T_N \simeq 1.1$ K. The ratio θ_{CW}/T_N is found to be quite large, making it convenient to investigate the magnetic properties over a wide range of temperatures.

II. METHODS

Synthesis of VO$(HCOO)_2 \cdot (H_2O)$ was performed following the conventional solvothermal route. In a typical reaction, 0.163 g (1 mmol) of $VOSO_4 \cdot (xH_2O)$ (Aldrich, 97%) and 6 ml (159 mmol) of formic acid (Spectrochem, 98%) were mixed and heated at 100 °C for three days in a teflon-lined stainless steel bomb of internal volume 20 mL. The resulting product was found to be a light blue powder that consists of plate-shaped crystals of the title compound. Single crystal x-ray diffraction (XRD) on a good quality single crystal confirms the orthorhombic (*Pcca*) crystal structure of the compound [26]. To further cross-check the phase purity, powder XRD was performed on the crushed powder sample at room temperature using a PANalytical (Cu K_α radiation, $\lambda_{ave} = 1.54182$ Å) powder diffractometer. Le Bail fit of the powder XRD pattern was performed using FULLPROF package [27], taking the initial structural parameters from Ref. [26]. Figure 2 presents the powder XRD pattern of VO$(HCOO)_2 \cdot (H_2O)$ at room temperature along with the fit. All the peaks could be fitted using the orthorhombic (*Pcca*) structure. The obtained best fit parameters are $a = 8.434(1)$ Å, $b = 7.4336(8)$ Å, $c = 8.4418(9)$ Å, and the goodness-of-fit $\chi^2 \simeq 6.68$. These lattice parameters are consistent with the earlier report [26].

Magnetic susceptibility χ was measured as a function of temperature (0.5 K $\leqslant T \leqslant$ 380 K) and applied magnetic field H. In the high-temperature range ($T \geqslant 2$ K), measurements were done using the vibrating sample magnetometer attachment to the Physical Property Measurement System (PPMS, Quantum Design). For $T \leqslant 2$ K, measurements were carried out using a ^{3}He attachment to the SQUID magnetometer (MPMS-7, Quantum Design). High field magnetization (M vs H) was measured at $T = 1.5$ K in pulsed magnetic field up to 40 T at the Dresden High Magnetic Field Laboratory. Heat capacity, $C_p(T)$ was also measured using the heat capacity option of the PPMS on a sintered pellet (annealed at 100 °C). For the low temperature (0.35 K $\leqslant T \leqslant$ 2 K) C_p measurements, an additional ^{3}He attachment was used in the PPMS. Since the size of the single crystals were very small, all measurements

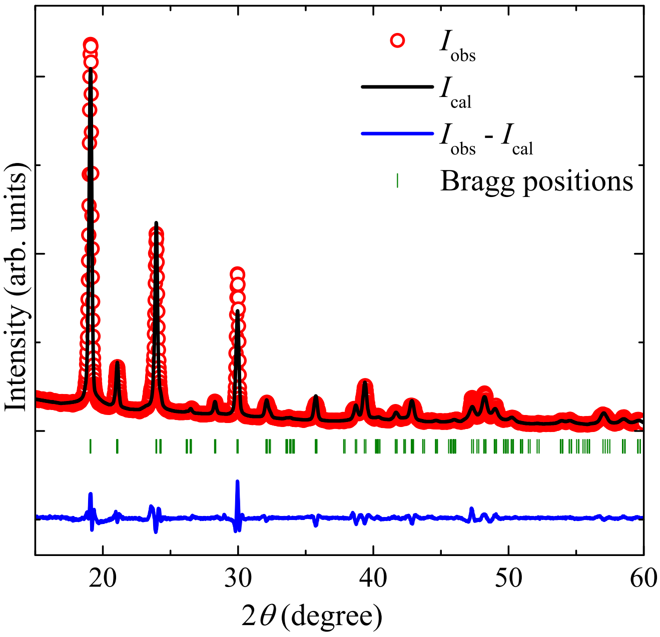

FIG. 2. Powder XRD pattern (open circles) at room temperature for $VO(HCOO)_2 \cdot (H_2O)$. The solid line is the Le Bail fit, the vertical bars represent the expected Bragg peak positions, and the lower solid line corresponds to the difference between the observed and calculated intensities.

were carried out on the powder sample, obtained by crushing a large number of single crystals.

The ESR experiments were carried out on a powder sample with a standard continuous-wave spectrometer in the temperature range 3 K $\leqslant T \leqslant$ 300 K. The power P absorbed by the sample from a transverse magnetic microwave field (X band, $\nu \simeq 9.4$ GHz) was measured as a function of the external magnetic field H. The final data were recorded as the derivative dP/dH with H. The ESR g-factor was estimated using the resonance condition $g = \frac{h\nu}{\mu_B H_{res}}$, where h is the Planck's constant, μ_B is the Bohr magneton, ν is the resonance frequency, and H_{res} is the corresponding resonance field.

For comparison with theory, quantum Monte Carlo (QMC) simulation for magnetization was performed assuming the Heisenberg model on a nonfrustrated square lattice with Hamiltonian $\mathcal{H} = J\sum_{ij}\vec{S}_i \cdot \vec{S}_j - H\sum_i S_i^z$, where J is the exchange coupling between spins at the ith and jth sites and H is magnetic field strength. We used the ALPS [28] code for the directed loop QMC algorithm in the stochastic series expansion representation [29]. The lattice size was taken to be 40 × 40. We typically did 10^5 sweeps, including around 5000 number of thermalization sweeps.

III. RESULTS

A. Magnetization

Temperature-dependent magnetic susceptibility $\chi(T)$ measured in an applied field of $H = 1$ T is shown in the upper panel of Fig. 3. As the temperature is lowered, $\chi(T)$ increases in a Curie-Weiss (CW) manner and then shows a broad maximum (T_χ^{max}) at about 10 K. This broad maximum is suggestive of a short-range magnetic order which is also a hallmark of low dimensionality. It exhibits a weak cusp at $T_N \simeq 1.1$ K, a possible indication of the occurrence of a magnetic LRO. With further reduction in temperature, a small upturn was observed which is likely due to the defects present in the sample. The inset of Fig. 3 shows $d\chi/dT$ vs T in the low-temperature regime to highlight the weak cusp associated with T_N.

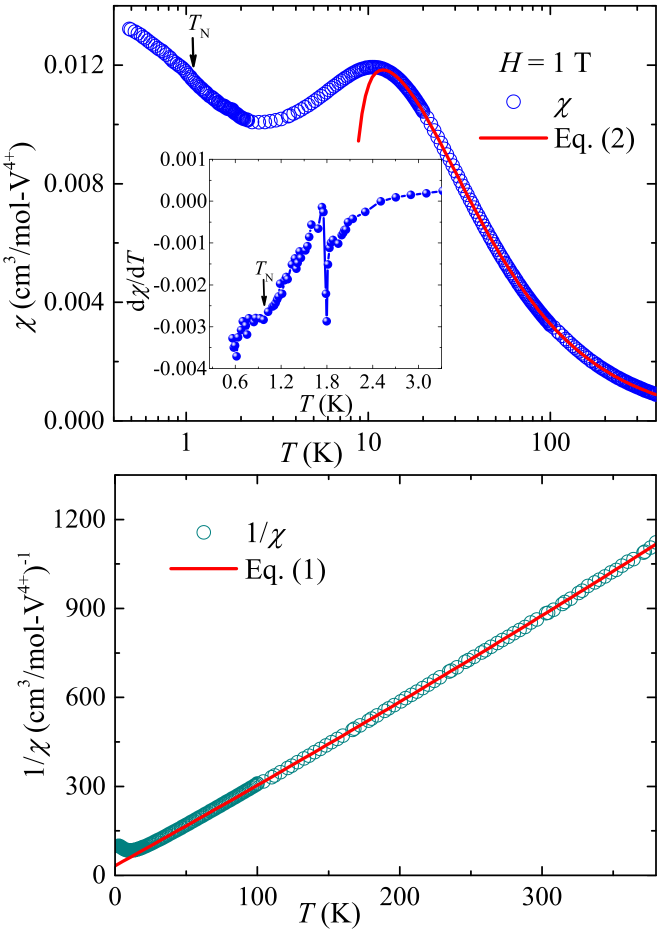

FIG. 3. Upper panel: $\chi(T)$ measured in an applied field of $H = 1$ T. Solid line represents the fit using 2D frustrated square lattice model [Eq. (2)]. Inset: $d\chi/dT$ vs T in the low-temperature regime to highlight T_N. The change of slope or discontinuity in $d\chi/dT$ at $T = 1.8$ K is related to the mismatch of data while switching from ^{4}He to ^{3}He attachment. Lower panel: Inverse magnetic susceptibility ($1/\chi$) at $H = 1$ T as a function of T. Solid line is the fit by Eq. (1).

For extracting the magnetic parameters, $\chi(T)$ at high temperatures was fitted by the following expression:

$$\chi(T) = \chi_0 + \frac{C}{T - \theta_{CW}}, \quad (1)$$

where χ_0 is the temperature-independent susceptibility consisting of core diamagnetism of the core electron shells and Van-Vleck paramagnetism of the open shells of the V^{4+} ions in the sample. The second term in Eq. (1) is the CW law with the CW temperature (θ_{CW}) and Curie constant $C = N_A\mu_{eff}^2/3k_B$, where N_A is Avogadro's number, k_B is Boltzmann constant, $\mu_{eff} = g\sqrt{S(S+1)}\mu_B$ is the effective magnetic moment, g is the Landé g-factor, μ_B is the Bohr magneton, and S is the spin quantum number.

Our fit in the temperature range 110 K to 380 K (lower panel of Fig. 3) yields $\chi_0 \simeq -6.363 \times 10^{-5}$ cm^3/mol-V^{4+}, $C \simeq 0.376$ cm^{3}K/mol-V^{4+}, and $\theta_{\rm CW} \simeq -12$ K. From the value of C, the effective moment is calculated to be $\mu_{\rm eff} \simeq 1.73\ \mu_{\rm B}/{\rm V}^{4+}$ which exactly matches with the expected spin-only value for $S = 1/2$ with $g = 2$. The negative value of $\theta_{\rm CW}$ is indicative of the AFM exchange interaction among the V^{4+} ions [30].

To understand the exchange network, the experimental $\chi(T)$ data were fitted by the equation

$$\chi(T) = \chi_0 + \chi_{\rm spin}(T). \tag{2}$$

Here, $\chi_{\rm spin}(T)$ is the high-temperature series expansion (HTSE) of spin susceptibility for the spin-1/2 frustrated square lattice (FSL) or $J_1 - J_2$ model [31,32]. The expression is given by

$$\chi_{\rm spin}(T) = \frac{N_A g^2 \mu_B^2}{k_B T} \sum_n \left(\frac{J_1}{k_B T}\right)^n \sum_m c_{m,n} \left(\frac{J_2}{J_1}\right)^m, \tag{3}$$

where, $c_{m,n}$ are the coefficients listed in Table I of Ref. [31]. This HTSE is valid only in the high-temperature region $T \geqslant J_i$. We fitted the experimental $\chi(T)$ data by Eq. (2) in the temperature range 12 K to 380 K fixing $g = 2$, obtained from the ESR experiments. It yields two solutions with equally good fits. Solution I: $\chi_0 \simeq -6.846 \times 10^{-5}$ cm^3/mol-V^{4+}, $J_1/k_{\rm B} \simeq 11.7$ K, and $J_2/k_{\rm B} \simeq 0.02$ K and solution II: $\chi_0 \simeq -6.936 \times 10^{-5}$ cm^3/mol-V^{4+}, $J_1/k_{\rm B} \simeq 11.7$ K, and ferromagnetic $J_2/k_{\rm B} \simeq -0.02$ K. In both solutions, the magnitude of J_2 is almost three orders of magnitude smaller or almost negligible compared to J_1, as is expected from the structural data. This also implies that the system can be viewed as a nonfrustrated square lattice. Since for a FSL, $\theta_{\rm CW} = J_1 + J_2$, our experimentally obtained higher value of $\theta_{\rm CW}$ favours solution-I with AFM J_1 and J_2. Nevertheless, in both the cases the J_1 and J_2 values locate the system in the Néel antiferromagnetic (NAF) region of the $J_1 - J_2$ phase diagram [7].

As observed from the $\chi(T)$ and zero-field $C_{\rm p}(T)$ data, the compound undergoes a magnetic LRO at $T_{\rm N} \simeq 1.1$ K. This suggests that there are non-negligible interplane couplings in contrast to what was expected from the structural data. From the value of $T_{\rm N}$, J_1, and J_2, one can calculate the average interplane coupling $J_\perp$ using the relation [33,34]

$$k_{\rm B}T_{\rm N} \simeq \pi(J_1 - 2J_2)/[2 + \ln((J_1 - 2J_2)/J_\perp)], \tag{4}$$

where nonfrustrated interlayer couplings are assumed. Taking the appropriate values ($T_{\rm N} \simeq 1.1$ K, $J_1/k_{\rm B} \simeq 11.7$ K, and $J_2/k_{\rm B} \simeq 0.02$ K), $J_\perp/k_{\rm B}$ is calculated to be $J_\perp/k_{\rm B} \simeq 3.3 \times 10^{-13}$ K. This value of $J_\perp/k_{\rm B}$ is found to be unrealistically low and even several orders of magnitude smaller than the dipole-dipole coupling. Such a discrepancy could be due to the bilayer nature of the spin-lattice and the presence of interlayer frustration.

To check whether there are any field-induced effects and to obtain the saturation magnetization, high-field magnetization was measured at $T = 1.5$ K up to 40 T. Figure 4 presents the magnetization (M) vs H normalized to one. At the low-field regime, M increases almost linearly with H and then shows a pronounced curvature before it saturates completely at $H_{\rm S} \simeq 32$ T. Such a pronounced curvature is indicative of strong quantum fluctuations or frustration in the spin system. The inset of Fig. 4 presents the derivative dM/dH as a function of H to magnify the change in slope at the saturation field $H_{\rm S}$. To reconfirm the magnitude of exchange couplings, we analyzed the value of the saturation field $H_{\rm S}$. According to theoretical results by Schmidt *et al.* [35], the saturation field in a FSL model can be calculated as

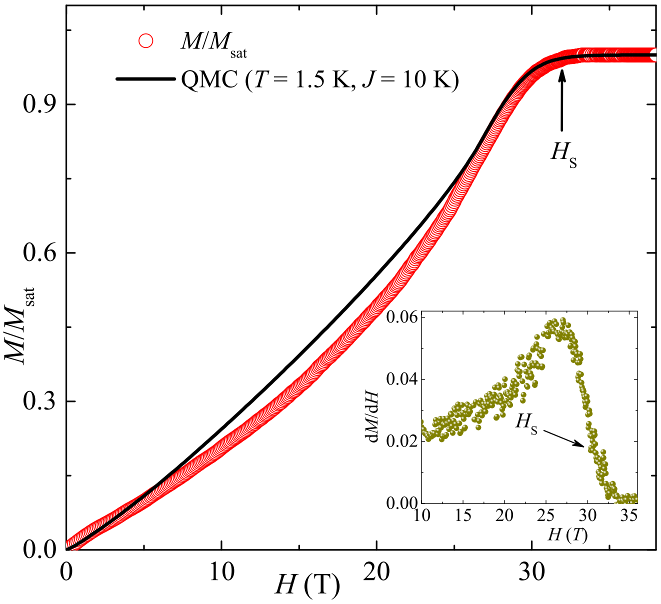

FIG. 4. Magnetization (normalized to one) vs field measured at $T = 1.5$ K. The solid line represents the QMC simulation, assuming a uniform square lattice model. Inset: dM/dH vs H highlighting the saturation field.

$$H_S = \frac{J_c k_B z S}{g\mu_B}\left[\left(1 - \frac{1}{2}(\cos Q_x + \cos Q_y)\right)\cos\varphi + (1 - \cos Q_x \cos Q_y)\sin\varphi\right], \tag{5}$$

where $z = 4$ (magnetic coordination number), $S = 1/2$, angle $\phi = \tan^{-1}(J_2/J_1)$, $J_{\rm c} = \sqrt{J_1^2 + J_2^2}$, and (Q_x, Q_y) is the wave vector of the ordered state. Using the appropriate wave vectors for the NAF (π, π) phase, one can have $H_S = 4J_1k_B/(g\mu_B)$. Using this formula, our experimental value of $H_{\rm S} \simeq 32$ T corresponds to $J_1/k_{\rm B} \simeq 10.7$ K, which is slightly smaller than the one (∼11.7 K) obtained from the $\chi(T)$ analysis.

B. ESR

The ESR experimental results on the VO(HCOO)$_2 \cdot$ (H$_2$O) powder sample are presented in Fig. 5. The lower inset of Fig. 5 illustrates a typical ESR spectrum at room temperature. We fitted the spectra using a powder-averaged Lorentzian line shape. The fit reproduces the spectral shape very well at $T = 300$ K, yielding anisotropic g-factors: parallel component $g_\parallel \simeq 1.97$ and perpendicular component $g_\perp \simeq 2.01$. The isotropic g-value $[= \sqrt{(g_\parallel^2 + 2g_\perp^2)/3}]$ is calculated to be $g \simeq 2.0$. As shown in the lower panel of Fig. 5, both $g_\parallel$ and $g_\perp$ are temperature independent in the high-temperature range. The line width at half maximum (ΔH) is also found to be

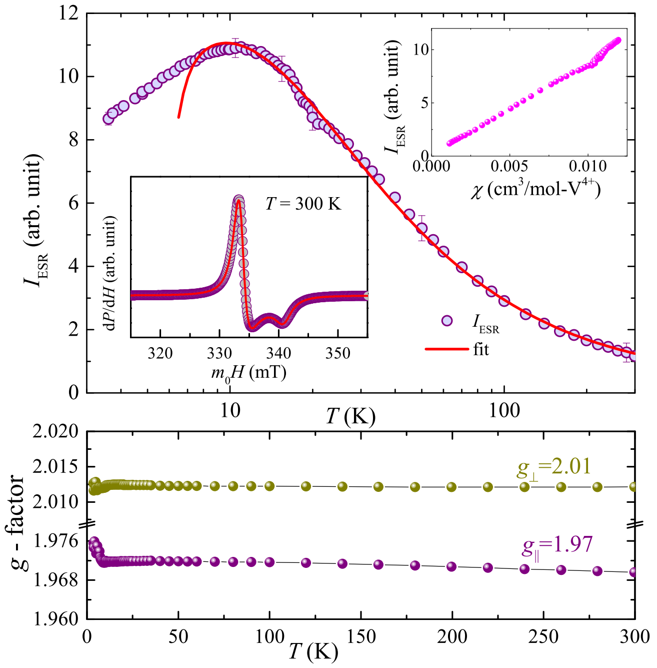

FIG. 5. Upper panel: Temperature-dependent ESR intensity, $I_{ESR}(T)$, obtained by integration of the ESR spectra of the polycrystalline sample. The solid line represents the fit described in the text. Lower inset: A typical spectrum (symbols) together with the fit using a powder-averaged Lorentzian shape for a uniaxial g-factor anisotropy. Top inset: I_{ESR} vs χ. Lower panel: Temperature-dependent g-factor ($g_\parallel$ and $g_\perp$) obtained from the Lorentzian fit.

temperature independent at high temperatures. For $T < 8$ K, both $\Delta H(T)$ and $g(T)$ show a gradual increase reflecting the appearance of spin correlations coming from the magnetic LRO at low temperatures. The ESR intensity (I_{ESR}) as a function of temperature shows a broad maximum at ∼10 K similar to the bulk $\chi(T)$ data. In the upper inset of Fig. 5, I_{ESR} is plotted as a function of χ. Indeed a linear behavior is observed over the whole measured temperature range providing clear evidence that $I_{ESR}(T)$ probes $\chi(T)$.

To estimate the exchange coupling, $I_{ESR}(T)$ data were fitted by the equation

$$I_{ESR} = A + B\chi_{spin}(T), \tag{6}$$

where A and B are constants and χ_{spin} is given in Eq. (3). The fit in the range 13 K to 380 K (upper panel of Fig. 5) yields $J_1/k_B \simeq 10.2$ K and $J_2/k_B \simeq 0.007$ K, fixing $g = 2$. These values of exchange couplings are close to the ones obtained from the high-field data but slightly smaller in magnitude than the ones obtained from the $\chi(T)$ analysis.

C. Heat capacity

The heat capacity C_p measured in zero applied field is shown in the upper panel of Fig. 6. In a magnetic insulator, C_p has two major contributions: one from phonon excitations (C_{ph}) and the other one is from the magnetic lattice (C_{mag}). At high temperatures, $C_p(T)$ is completely dominated by the contribution of C_{ph} while at low temperatures, it is dominated by C_{mag}. Our $C_p(T)$ data show a weak broad maximum at $T_C^{max} \simeq 8.5$ K, similar to that observed in $\chi(T)$. A weak and slightly broad anomaly is detected at around $T_N \simeq 1.1$ K associated with the magnetic LRO. With further decrease in T, $C_p(T)$ decreases gradually toward zero.

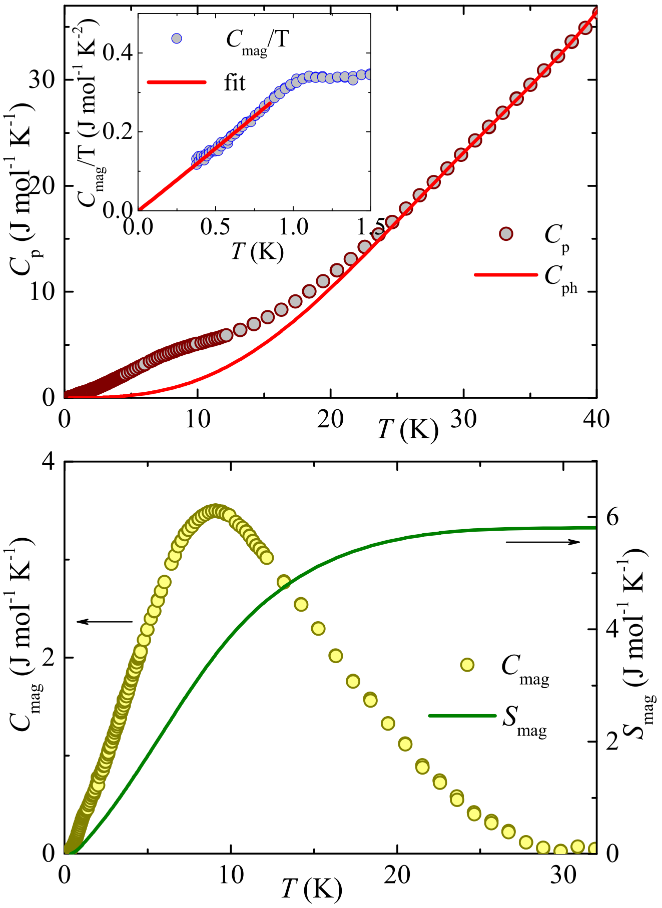

FIG. 6. Upper panel: Heat capacity $C_p(T)$ of $VO(HCOO)_2 \cdot (H_2O)$ measured in zero applied field along with the calculated $C_{ph}(T)$. Inset: C_{mag}/T vs T and the solid line is a linear fit. Lower panel: C_{mag} (left y axis) and S_{mag} (right y axis) are plotted as a function of T.

To estimate the phonon part of the heat capacity, $C_p(T)$ data at high temperature ($T > 25$ K) were fitted by the polynomial

$$C_{ph}(T) = aT^3 + bT^5 + cT^7 + dT^9, \tag{7}$$

where a, b, c, and d are arbitrary constants [36]. A similar procedure has been adopted earlier and proven to be an efficient method for the estimation of C_{ph} in the case of metal-organic complexes [16,20,37]. The fit was extrapolated down to low temperatures and the C_{mag} was obtained by subtracting the fitted data from the experimental C_p data. To check the reliability of the fitting procedure, we calculated the total change in magnetic entropy (S_{mag}) by integrating $C_{mag}(T)/T$ from 0.35 K to high temperatures as $S_{mag}(T) = \int_{0.35\,K}^{T} \frac{C_{mag}(T')}{T'} dT'$. The resulting magnetic entropy is $S_{mag} \simeq 5.8$ J/mol K at 30 K. This value reasonably matches with the expected theoretical value [$S_{mag} = R\ln(2S+1)$] of 5.76 J/mol K for $VO(HCOO)_2 \cdot (H_2O)$. The obtained $C_{mag}(T)$ is presented in the lower panel of Fig. 6. Below T_N, $C_{mag}(T)$

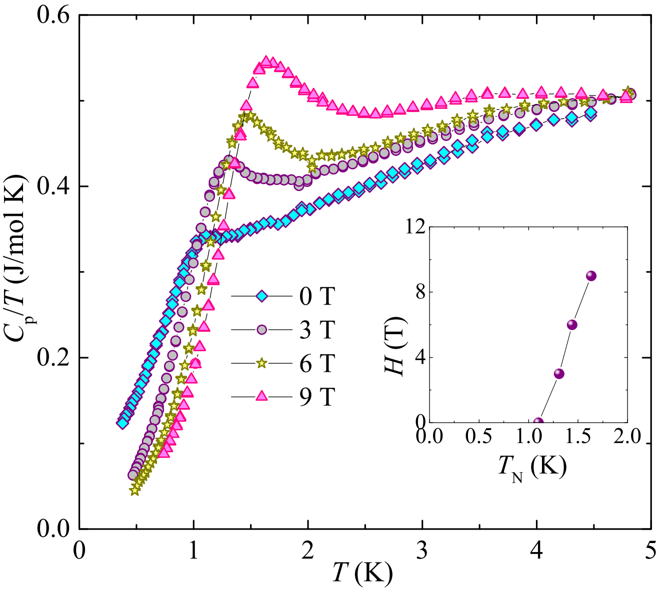

FIG. 7. C_p/T measured in different applied magnetic fields in the low-temperature region. Inset: The variation of T_N with H.

follows a power law T^{α} with a reduced exponent $\alpha \simeq 2$ (see the inset of the upper panel of Fig. 6).

To understand the nature of ordering at T_N, $C_p(T)$ of $VO(HCOO)_2 \cdot (H_2O)$ was measured in different applied magnetic fields (see Fig. 7). With increasing magnetic field, the peak height at T_N is found to be increasing and the peak position is shifting toward higher temperatures. This behavior is just opposite to what is expected for an AFM 3D ordering. In the inset of Fig. 7, T_N vs H is plotted. T_N varies almost linearly with H up to the maximum measured field of 9 T.

IV. DISCUSSION

A most obvious feature of low-dimensional AFM spin systems is the occurrence of short-range order. Thus, the appearance of broad maximum in $\chi(T)$ and $C_p(T)$ clearly suggests a quasi-2D character of the compound. Our experimental $\chi(T)$ data agree well with the HTSE for the spin-1/2 2D FSL model. Further confirmation about the two-dimensionality can be obtained from the analysis of C_{mag}. In low-dimensional spin systems, the absolute value of C_{mag} at the maximum (C_{mag}^{max}) and the shape of the maximum are representative measures of dimensionality or quantum fluctuations and the temperature corresponding to the maximum (T_C^{max}) uniquely determines the exchange coupling [45,46]. With reduced dimensionality, the quantum fluctuations are enhanced, which apparently suppresses the correlated spin excitations, leading to a reduction in C_{mag}^{max} and broadening of the maximum. For instance, in a nonfrustrated 2D square lattice, a relatively higher value $C_{mag}^{max} \simeq 0.46R = 3.82$ J/mol K is expected at $T_C^{max}/J_{2D} = 0.60$ [2,47,48]. In case of uniform one-dimensional (1D) spin chains where the quantum fluctuations are more, this value decreases to $C_{mag}^{max} \simeq 0.35R = 2.9$ J/mol K at $T_C^{max}/J_{1D} = 0.48$ with a broad distribution [46,49]. On the other hand, the triangular lattice (a frustrated 2D lattice) which is highly frustrated shows an even lower ($C_{mag}^{max} \simeq 0.22R = 1.83$ J/mol K) value and broader maximum compared to uniform chains [46]. The effect of magnetic frustration not only suppresses the absolute value but also shifts the maximum toward lower temperatures. Clearly, our experimental value of $C_{mag}^{max} \simeq 3.6$ J/mol K is more close to the one expected for the 2D square lattice model but much larger than the 1D model. This is a definite confirmation of the 2D character of the compound and a small reduction in the experimental C_{mag} value could be due to the bilayer nature of the spin lattice and the effect of magnetic frustration.

To further justify the spin lattice, QMC simulation was performed to simulate M as a function of H and compared with the experimental data at $T = 1.5$ K. The simulation was done assuming a pure 2D square lattice with no interlayer couplings. For $J/k_B = 10$ K, the simulation closely reproduces our experimental curve, especially in the low- and high-field regimes, implying that the spin lattice is a 2D square lattice. However, a clear departure from the experimental data is noticed in the intermediate field range. This is because our simulation is done assuming a purely nonfrustrated square-lattice model without any interlayer couplings. As pointed out earlier, there are weak interlayer couplings which are making a frustrated geometry. Thus, the curvature in the M vs H curve could be attributed to this frustration effect and/or spatial anisotropy in the *ac* plane which cannot be assessed from the magnetization data on the powder sample [9].

As shown in the inset of Fig. 7, T_N shifts toward high temperatures almost linearly with increasing field in contrast to what is expected for a typical 3D AFM ordering. In several frustrated low-dimensional compounds, it is observed that when magnetic field is applied, initially T_N moves slightly toward high temperatures. With further increase in field, it shifts back to low temperatures and reaches the fully polarized state [9,10,45,50]. Indeed, the recent theoretical study by Schmidt and Thalmeier [34], which reports the full phase diagram for all the frustration ratios of a quasi-2D frustrated magnet, produces an identical shape. It is suggested that the sublattice moment in low-dimensional frustrated spin systems is usually suppressed by quantum fluctuations. Magnetic field suppresses these fluctuations, thereby gradually restoring the sublattice moment and enhancing T_N slightly at low fields. When the field is strong enough to overcome the AFM ordering, T_N is reduced; as a result, a belly shaped $H - T$ phase diagram is formed. However, in our compound, T_N shows a steady increase even up to a high field of 9 T which cannot be attributed to the effect of quantum fluctuations alone. The observed trend in the $H - T$ phase diagram could also be due to strong in-plane anisotropy in the present compound, as expected from the crystal structure. Nevertheless, our observation resembles the field-induced behavior reported in spin-1/2 square lattices $Pb_2Cu(OH)_4Cl_2$ and $Cu(pz)_2(ClO_4)_2$ with strong in-plane anisotropy [18,51,52].

Moreover, in an AFM ordered state, one would expect a power law (T^{α}) behavior for $C_{mag}(T)$ due to the spin wave excitations. For a 3D system, the exponent has a value $\alpha = 3$ [53,54]. On the other hand, for a 2D system, these excitations have a linear k dependence around the Bragg points, leading to a T^2 dependence of C_{mag} [55]. Similarly, for a 1D Heisenberg spin chain, $C_{mag}(T)$ follows a linear behavior with temperature, below T_N. In our compound, $C_{mag}(T)$

TABLE I. Comparison of the magnetic parameters of $VO(HCOO)_2 \cdot (H_2O)$ with different reported spin-1/2 2D layered metal-organic compounds. Since θ_{CW} for all the compounds is not available in the literature, for a quantitative comparison, we have tabulated both the θ_{CW}/T_N and J_1/T_N ratios.

Compounds	θ_{CW} (K)	J_1/k_B (K)	T_N (K)	θ_{CW}/T_N	J_1/T_N	Refs.
$VO(HCOO)_2 \cdot (H_2O)$	12	11	1.1	10.9	10	this paper
$Cu(PM)(EA)_2$	3	6.8	–	–	–	[16]
$Cu(COOH)_2 \cdot 4H_2O$	150	73	16.5	9.1	4.42	[17,38]
$Cu(COOH)_2 \cdot 2CO(NH_2)_2 \cdot 2H_2O$	–	70	15.5	–	4.5	[39]
$CuF_2 \cdot 2H_2O$	37	26	10.9	3.39	2.38	[40,41]
$[Cu(C_5H_5NO)_6][BF_4]_2$	–	1.1	0.62	–	1.77	[42]
$Cu(Pz)_2(ClO_4)_2$	23.8	17.7	4.21	5.67	4.2	[20,43]
$[Cu(Pz)_2(HF_2)]BF_4$	8.1	2.85	1.54	5.25	1.8	[44]
$(5MAP)_2CuBr_4$	–	6.5	3.8	–	1.71	[41]
$(5CAP)_2CuBr_4$	–	8.5	5.08	–	1.67	[41]
$(5CAP)_2CuCl_4$	–	1.14	0.74	–	1.54	[41]
$(5MAP)_2CuCl_4$	–	0.76	0.44	–	1.72	[41]

below T_N indeed follows a T^α behavior with a reduced exponent $\alpha \simeq 2$. This observed quadratic T-dependence indicates the dominance of 2D AFM spin waves, below T_N [56]. Finally, we made a comparison of our system with other reported compounds. Table I summarizes the number of spin-1/2 metal-organic compounds with 2D geometry. Clearly, $VO(HCOO)_2 \cdot (H_2O)$ has the largest $\frac{\theta_{CW}}{T_N}$ or $\frac{J_1}{T_N}$ ratio compared to other compounds, making it the best example of a metal-organic-based quasi-2D square lattice compound so far.

V. CONCLUSION

$VO(HCOO)_2 \cdot (H_2O)$ is realized to be an exotic double-layered square-lattice compound. The magnetic susceptibility, heat capacity, and high-field-magnetization data could be described well by a spin-1/2 FSL model without any substantial in-plane frustration and consistently produce the intralayer coupling $J_1/k_B = (11 \pm 1)$ K. The saturation of exchange couplings at $H_S \simeq 32$ T further confirms the magnitude of J_1. The onset of a magnetic LRO at a relatively low temperature $T_N \simeq 1.1$ K is ascribed to weak and frustrated interlayer couplings. A much higher value of $\theta_{CW}/T_N \simeq 10.9$ or $J_1/T_N \simeq 10$ compared to other 2D compounds makes $VO(HCOO)_2 \cdot (H_2O)$ the best experimental realization of a quasi-2D square lattice so far among the metal-organic complexes. The T^2 dependence of C_{mag} at low temperatures further reflects the dominant role of 2D AFM magnons below T_N. Moreover, the disagreement of the high-field magnetization data in the intermediate field range with that of the QMC simulation at low temperature can be attributed to the bilayered geometry and the effect of interlayer frustration.

ACKNOWLEDGMENTS

U.A., S.G., and R.N. would like to acknowledge BRNS, India for financial support bearing Sanction No. 37(3)/14/26/2017-BRNS. A.T. also acknowledges the financial support from SERB, India for the grant EMR/2016/002637.

[1] E. Manousakis, Rev. Mod. Phys. **63**, 1 (1991).
[2] M. S. Makivić and H.-Q. Ding, Phys. Rev. B **43**, 3562 (1991).
[3] J.-K. Kim and M. Troyer, Phys. Rev. Lett. **80**, 2705 (1998).
[4] A. W. Sandvik, Phys. Rev. B **56**, 11678 (1997).
[5] N. D. Mermin and H. Wagner, Phys. Rev. Lett. **17**, 1133 (1966).
[6] C. Yasuda, S. Todo, K. Hukushima, F. Alet, M. Keller, M. Troyer, and H. Takayama, Phys. Rev. Lett. **94**, 217201 (2005).
[7] N. Shannon, B. Schmidt, K. Penc, and P. Thalmeier, Eur. Phys. J. B **38**, 599 (2004).
[8] N. Shannon, T. Momoi, and P. Sindzingre, Phys. Rev. Lett. **96**, 027213 (2006).
[9] R. Nath, A. A. Tsirlin, H. Rosner, and C. Geibel, Phys. Rev. B **78**, 064422 (2008).
[10] R. Nath, Y. Furukawa, F. Borsa, E. E. Kaul, M. Baenitz, C. Geibel, and D. C. Johnston, Phys. Rev. B **80**, 214430 (2009).
[11] N. Tsyrulin, T. Pardini, R. R. P. Singh, F. Xiao, P. Link, A. Schneidewind, A. Hiess, C. P. Landee, M. M. Turnbull, and M. Kenzelmann, Phys. Rev. Lett. **102**, 197201 (2009).
[12] P. A. Lee, Rep. Prog. Phys. **71**, 012501 (2007).
[13] A. Jain, M. Krautloher, J. Porras, G. Ryu, D. Chen, D. Abernathy, J. Park, A. Ivanov, J. Chaloupka, G. Khaliullin, B. Keimer, and B. Kim, Nat. Phys. **13**, 633 (2017).
[14] D. Pekker and C. Varma, Annu. Rev. Condens. Matter Phys. **6**, 269 (2015).
[15] P. A. Goddard, J. L. Manson, J. Singleton, I. Franke, T. Lancaster, A. J. Steele, S. J. Blundell, C. Baines, F. L. Pratt, R. D. McDonald, O. E. Ayala-Valenzuela, J. F. Corbey, H. I. Southerland, P. Sengupta, and J. A. Schlueter, Phys. Rev. Lett. **108**, 077208 (2012).
[16] R. Nath, M. Padmanabhan, S. Baby, A. Thirumurugan, D. Ehlers, M. Hemmida, H.-A. Krug von Nidda, and A. A. Tsirlin, Phys. Rev. B **91**, 054409 (2015).
[17] H. M. Rønnow, D. F. McMorrow, R. Coldea, A. Harrison, I. D. Youngson, T. G. Perring, G. Aeppli, O. Syljuåsen, K. Lefmann, and C. Rischel, Phys. Rev. Lett. **87**, 037202 (2001).

[18] N. Tsyrulin, F. Xiao, A. Schneidewind, P. Link, H. M. Rønnow, J. Gavilano, C. P. Landee, M. M. Turnbull, and M. Kenzelmann, Phys. Rev. B **81**, 134409 (2010).

[19] M. Siahatgar, B. Schmidt, and P. Thalmeier, Phys. Rev. B **84**, 064431 (2011).

[20] T. Lancaster, S. J. Blundell, M. L. Brooks, P. J. Baker, F. L. Pratt, J. L. Manson, M. M. Conner, F. Xiao, C. P. Landee, F. A. Chaves, S. Soriano, M. A. Novak, T. P. Papageorgiou, A. D. Bianchi, T. Herrmannsdörfer, J. Wosnitza, and J. A. Schlueter, Phys. Rev. B **75**, 094421 (2007).

[21] S. Lefebvre, P. Wzietek, S. Brown, C. Bourbonnais, D. Jérome, C. Mézière, M. Fourmigué, and P. Batail, Phys. Rev. Lett. **85**, 5420 (2000).

[22] M.-S. Nam, A. Ardavan, S. J. Blundell, and J. A. Schlueter, Nature **449**, 584 (2007).

[23] K. Y. T. Ishiguro and G. Saito, *Organic Superconductors*, 2nd ed. (Springer, Berlin, 2006).

[24] R. S. Manna, M. de Souza, A. Brühl, J. A. Schlueter, and M. Lang, Phys. Rev. Lett. **104**, 016403 (2010).

[25] D. Mootz and R. Seidel, Acta Crystallogr., Sect. C **43**, 1218 (1987).

[26] T. R. Gilson, J. Solid State Chem. **117**, 136 (1995).

[27] J. Rodríguez-Carvajal, Physica B: Condens. Matter **192**, 55 (1993).

[28] ALPS project, http://alps.comp-phys.org/.

[29] A. W. Sandvik, Phys. Rev. B **59**, R14157 (1999); F. Alet, S. Wessel, and M. Troyer, Phys. Rev. E **71**, 036706 (2005); L. Pollet, S. M. A. Rombouts, K. Van Houcke, and K. Heyde, *ibid.* **70**, 056705 (2004).

[30] C. Domb and A. R. Miedema, *Progress in Low Temperature Physics*, edited by C. J. Gorter, Vol. 4 (North Holland, Amsterdam, 1964).

[31] H. Rosner, R. R. P. Singh, W. H. Zheng, J. Oitmaa, and W. E. Pickett, Phys. Rev. B **67**, 014416 (2003).

[32] H.-J. Schmidt, A. Lohmann, and J. Richter, Phys. Rev. B **84**, 104443 (2011).

[33] N. Majlis, S. Selzer, and G. C. Strinati, Phys. Rev. B **45**, 7872 (1992).

[34] B. Schmidt and P. Thalmeier, Phys. Rev. B **96**, 214443 (2017).

[35] B. Schmidt, P. Thalmeier, and N. Shannon, Phys. Rev. B **76**, 125113 (2007).

[36] The fitting results in $a \simeq 18.35 \times 10^{-4}$ mol^{-1} K^{-4}, $b \simeq 1.61 \times 10^{-6}$ mol^{-1} K^{-6}, $c \simeq 6.70 \times 10^{-10}$ mol^{-1} K^{-8}, and $d \simeq 9.90 \times 10^{-14}$ mol^{-1} K^{-10}.

[37] T. Matsumoto, Y. Miyazaki, A. S. Albrecht, C. P. Landee, M. M. Turnbull, and M. Sorai, J. Phys. Chem. B **104**, 9993 (2000).

[38] H. Kobayashi and T. Haseda, J. Phys. Soc. Jpn. **18**, 541 (1963).

[39] K. Yamagata and H. Abe, J. Magn. Magn. Mater. **31–34**, 1179 (1983).

[40] S. C. Abrahams, J. Chem. Phys. **36**, 56 (1962).

[41] F. M. Woodward, A. S. Albrecht, C. M. Wynn, C. P. Landee, and M. M. Turnbull, Phys. Rev. B **65**, 144412 (2002).

[42] H. Algra, L. de Jongh, and R. Carlin, Physica B+C **93**, 24 (1978).

[43] F. M. Woodward, P. J. Gibson, G. B. Jameson, C. P. Landee, M. M. Turnbull, and R. D. Willett, Inorg. Chem. **46**, 4256 (2007).

[44] J. L. Manson, M. M. Conner, J. A. Schlueter, T. Lancaster, S. J. Blundell, M. L. Brooks, F. L. Pratt, T. Papageorgiou, A. D. Bianchi, J. Wosnitza, and M.-H. Whangbo, Chem. Commun. **0**, 4894 (2006).

[45] R. Nath, A. A. Tsirlin, E. E. Kaul, M. Baenitz, N. Büttgen, C. Geibel, and H. Rosner, Phys. Rev. B **78**, 024418 (2008).

[46] B. Bernu and G. Misguich, Phys. Rev. B **63**, 134409 (2001).

[47] M. Hofmann, T. Lorenz, K. Berggold, M. Grüninger, A. Freimuth, G. S. Uhrig, and E. Brück, Phys. Rev. B **67**, 184502 (2003).

[48] J. Oitmaa and E. Bornilla, Phys. Rev. B **53**, 14228 (1996).

[49] D. C. Johnston, R. K. Kremer, M. Troyer, X. Wang, A. Klümper, S. L. Bud'ko, A. F. Panchula, and P. C. Canfield, Phys. Rev. B **61**, 9558 (2000).

[50] L. J. de Jongh, *Magnetic Properties of Layered Transition Metal Compounds*, Vol. 9 (Springer, Dordrecht, 2012)

[51] A. A. Tsirlin, O. Janson, S. Lebernegg, and H. Rosner, Phys. Rev. B **87**, 064404 (2013).

[52] K. Y. Povarov, A. I. Smirnov, and C. P. Landee, Phys. Rev. B **87**, 214402 (2013).

[53] R. Nath, K. M. Ranjith, B. Roy, D. C. Johnston, Y. Furukawa, and A. A. Tsirlin, Phys. Rev. B **90**, 024431 (2014).

[54] J. A. Eisele and F. Keffer, Phys. Rev. **96**, 929 (1954).

[55] Y. Kitaoka, T. Kobayashi, A. Kōda, H. Wakabayashi, Y. Niino, H. Yamakage, S. Taguchi, K. Amaya, K. Yamaura, M. Takano, A. Hirano, and R. Kanno, J. Phys. Soc. Jpn. **67**, 3703 (1998).

[56] A. P. Ramirez, G. P. Espinosa, and A. S. Cooper, Phys. Rev. Lett. **64**, 2070 (1990).